International Journal of Hydrogen Energy 219 (2026) 154003

Contents lists available at ScienceDirect

International Journal of Hydrogen Energy

journal homepage: www.elsevier.com/locate/he

High-capacity and rapid hydrogen storage in 1,3-dioxolane-H_2 hydrate via pre-wetted bamboo charcoal

Zhongming Fan [a], Yanhong Wang [a], Xuemei Lang [a,b], Gang Li [a], Xinfa Dong [a,c], Shuanshi Fan [a,b,*]

[a] School of Chemistry and Chemical Engineering, South China University of Technology, Guangzhou, 510640, China
[b] Key Laboratory of Heat and Mass Transfer and Low-Carbon Conversion, Ministry of Education, South China University of Technology, Guangzhou, 510640, China
[c] Guangdong Provincial Key Laboratory of Green Chemical Product Technology, Guangzhou, 510640, China

ARTICLE INFO

Keywords:
DIOX-H_2 mixed hydrates
Hydrogen storage
Bamboo charcoal
Pre-wetted
Second-stage hydrogen injection

ABSTRACT

Hydrate-based hydrogen storage faces two persistent challenges: sluggish formation kinetics and low hydrogen storage capacity. Porous materials provide nucleation sites, while interconnected microchannels enhance hydrogen mass transfer to accelerate hydrate growth. Bamboo charcoal (BC) shows significant potential for advancing hydrate-based hydrogen storage capacity. In this work, BC pre-wetted with 1,3-dioxolane (DIOX) solution served as a dispersed porous medium. Using single-stage and second-stage injection, were induction-free formation of DIOX-H_2 hydrates with superior hydrogen storage performance. Second-stage hydrogen injection is proposed to enhance hydrogen storage density and accelerate storage rates under specified pressures, triggered when the reactor pressure falls below the set value. Second-stage injection increased hydrogen storage capacity by 30.92% compared to single-stage injection, reaching 0.726 wt% at 272.15 K and 18 MPa. An average storage rate of 0.952 wt%/h was attained in 0.5 h. To our knowledge, this system achieved the highest reported storage capacity (0.726 wt%) for DIOX-H_2 hydrates. A combination of microscopy, BET, Raman spectroscopy, FIIR and SEM was employed to analyze the morphological changes of the BC and the growth status of DIOX-H_2 hydrate within its channels. Microscopic observation revealed that the solution was uniformly distributed within the BC's pores, and the DIOX–H_2 hydrate exhibited a micrometer-scale film-like growth morphology. Raman spectroscopy analysis revealed the hydrogen cage occupancy behavior of DIOX–H_2 within the pores. The results successfully demonstrated the formation of DIOX-H_2 hydrate inside the BC's channels and elucidated that the enhanced hydrogen storage in hydrate is attributed to the increased gas-liquid contact area provided by the charcoal's porous structure. This work establishes a simple yet effective strategy to advance hydrate-based hydrogen storage technology.

1. Introduction

Hydrogen, a green energy carrier with high sustainability and an exceptional calorific value of 142 MJ/kg, holds broad application prospects. While current production technologies have matured [1], safety concerns persist during storage/transport due to hydrogen's low ignition point and wide flammability range (4-75 vol%) [2]. To address these risks, three primary storage strategies have emerged: cryogenic liquid, high-pressure gaseous, and solid-state storage [3]. However, High-pressure storage tanks for hydrogen are prone to hydrogen embrittlement, which can lead to hydrogen leakage [4]. Among these, hydrate-based hydrogen storage represents a particularly promising solid-state approach, offering exceptional safety advantages and substantial potential for practical implementation.

Hydrate-based hydrogen storage has garnered significant attention due to its inherent safety advantages [5], environmental compatibility [6], and rapid dehydrogenation kinetics [7]. This technology utilizes van der Waals forces between water molecules to form crystalline cages that physically encapsulate hydrogen. Given its capability in gas separation [8] and carbon capture [9], hydrate technology represents a highly promising pathway, one that is expected to deliver substantial economic and social value. Hydrates primarily exist as sI, sII and H-type structures [10], with sII-type hydrates being predominantly studied owing to their milder formation conditions and superior hydrogen

* Corresponding author. School of Chemistry and Chemical Engineering, South China University of Technology, Guangzhou, 510640, China.
E-mail address: ssfan@scut.edu.cn (S. Fan).

https://doi.org/10.1016/j.ijhydene.2026.154003
Received 20 November 2025; Received in revised form 21 January 2026; Accepted 9 February 2026
Available online 18 February 2026

storage capacity. The sII hydrate crystallizes in a face-centered cubic lattice (space group Fd3m), comprising 8 large cages ($5^{12}6^4$) and 16 small cages (5^{12}) within a 136-water-molecule framework. Hydrogen molecules preferentially occupy the 5^{12} small cages. Mao et al. [11] demonstrated pure hydrogen hydrates achieving storage densities up to 5.0 wt%. However, their formation demands extreme conditions, temperatures of 249 K coupled with pressures exceeding 180 MPa, rendering industrial implementation impractical.

To moderate the formation conditions of hydrogen hydrates, incorporating thermodynamic promoters has proven effective [12]. Common thermodynamic promoters for hydrate formation include tetrahydrofuran (THF) [2,13,14]-epoxycyclopentane (ECP) [15], and cyclopentane (CP) [16]. Additionally, 1,3-dioxolane (DIOX) is also widely used [17,18]. Promoters such as propane (C_3H_8) [19–22] and methane [23] are effective as well, with further studies supporting the efficacy of propane [24]. Besides, the structure of TBAB/SF_6 hydrate also exhibited outstanding hydrogen storage performance with the characteristics of two-step hydrate growth [25]. Florusse et al. [13] demonstrated that THF addition elevates hydrate formation temperature to 279.6 K while reducing pressure to 5 MPa. Structurally analogous to THF, DIOX exhibits significantly lower volatility and toxicity [26,27] and functions as a dual-action promoter. However, Zhang et al. [28] and Kong et al. [29] revealed limitations in DIOX-H_2 mixed hydrates systems under stirred conditions, prolonged induction periods (>2 h), slow formation kinetics (40 h), and suboptimal storage densities (0.286 wt% and 0.430 wt%). Consequently, achieving efficient hydrogen storage in DIOX-H_2 mixed hydrates under static conditions remains unexplored. Static systems require optimized solution dispersion to prevent mass transfer limitations. Cryogenic pulverization—freezing solutions followed by grinding into ice powders-enhances gas-liquid interfaces, thereby improving storage capacity. Chen et al. [15] achieved 0.464 wt% storage after 40 h using 5.56 mol% ECP hydrate powders prepared at 243 K. Nevertheless, this approach suffers from slow kinetics and technical complexity. While reducing promoter dosage may be cost-beneficial, it makes the phase equilibrium conditions for hydrate formation more demanding. Furthermore, this reduction often overlooks the positive effect of increased solution dispersion on hydrogen storage capacity and the challenge of insufficient process driving force. Novel dispersion strategies that simultaneously enhance hydrogen storage density and accelerate kinetics are therefore imperative.

Porous materials have garnered significant research interest in recent years for their dual capability to accelerate hydrogen hydrate formation kinetics and enhance hydrogen storage density [30]. Functioning as efficient kinetic promoters, these materials feature intricate pore networks that disperse aqueous solutions to expand gas-liquid interfacial areas while providing abundant nucleation sites [30]. Representative porous systems applied in this field include hydrogels [31,32], stainless steel fibers [15,33], and cellulose matrices [34]. Metal-organic frameworks (MOFs) [35,36] and various activated carbons [37] have also been widely studied. Furthermore, mesoporous and metallic foams [38,39], along with silica gel [40,24], are commonly utilized. Organosilica nanoparticles represent another effective system [41]. Notably, Watson et al. [41] demonstrated that hydrophobic periodic mesoporous organosilica nanoparticles mixed with 5.56 mol% THF solution achieved 0.326 wt% storage at 265 K and 7 MPa within 4 h. Similarly, Lee et al. [31] employed superabsorbent polymers (SAPs, sodium polyacrylate) as porous substrates for THF dispersion, attaining 0.222 wt% storage at 274 K and 12 MPa in 3.3 h. However, the aforementioned methods all utilize very fine porous materials for hydrate-based hydrogen storage. Although these fine particles can disperse the solution and increase the gas-liquid contact area to a certain extent, they readily suspend at the gas-liquid interface, forming a powder-like film layer. Furthermore, the significant amount of solution trapped between particles creates mass transfer resistance for hydrogen, and their thermal conductivity is poor [42]. To address this, larger porous particles are needed to prevent aggregation and provide enhanced thermal conductivity for the timely removal of hydrate formation heat. Bamboo charcoal (BC), as a biocompatible porous material, is widely available and possesses abundant multi-sized pores along with good thermal conductivity [43]. On one hand, the solution can be dispersed within the BC pores to increase the gas-liquid contact area and promptly remove the heat generated during hydrogen hydrate formation. On the other hand, the larger particles size of BC prevent spontaneous aggregation under static conditions, thereby avoiding obstruction of the hydrogen mass transfer process. Consequently, utilizing larger BC particles is expected to effectively prevent particle aggregation while simultaneously dispersing the solution and facilitating heat removal, thereby accelerating the hydrogen storage rate and increasing the hydrogen storage density within DIOX-H_2 mixed hydrates.

To address the challenges of low hydrogen storage density and slow kinetics in hydrate-based hydrogen storage technology, BC particles with a size range of 6~12 mm were employed as the porous material, utilizing 1,3-dioxane (DIOX) as a promoter. A novel pre-wetting via immersion (IP) method for BC-enhanced DIOX-H_2 mixed hydrates formation was proposed. Comparative analysis revealed that this pre-wetted BC approach significantly enhanced both the hydrogen storage density within the hydrate and the hydrogen uptake rate compared to the conventional method of simply mixing the solution with BC particles. Subsequently, to further increase the storage density, a second-stage hydrogen injection strategy was implemented to augment the driving force during the later stages of the storage process. Second-stage hydrogen injection is proposed to enhance hydrogen storage density and accelerate storage rates under specified pressures, triggered when the reactor pressure falls below the set value. This successfully enabled highly efficient DIOX hydrate-based hydrogen storage. Finally, morphological characterization of the BC before and after hydrate formation was conducted to elucidate the promotion mechanism of the pre-wetting via immersion method. This finding is anticipated to facilitate the practical implementation of hydrate-based hydrogen storage technology.

2. Experimental

2.1. Materials

High-purity hydrogen gas (>99.99%) was supplied by Kede Gas Chemical Co., Ltd. (Foshan, China). BC particles with a size range of 6~12 mm were purchased from Yiyang Kechen Trading Co., Ltd. (Yiyang, China), exhibiting an average dead volume density of 0.853 $cm^3\ g^{-1}$ 1,3-Dioxane (DIOX) with a purity of 99.5% was obtained from Beijing Innochem Science & Technology Co., Ltd. (Beijing, China, https://www.inno-chem.com.cn/). The Deionized water used throughout the experiments was produced in the laboratory.

The surface morphology and pore structure of the BC were characterized using scanning electron microscopy (SEM). Observations were performed using a benchtop SEM instrument (EM-30 Plus, COXEM Co., Ltd.) operating in high-vacuum secondary electron imaging mode with a resolution of ≤5 nm. The instrument employed a tungsten filament emission source operating at 30 kV. The achievable magnification range was 20 × to 150,000 × , with an adjustable accelerating voltage spanning 1 kV to 30 kV.

The N_2 adsorption isotherm measurements for the BC were conducted at 77 K using a BSD-660S A3 analyzer (Beishide Instrument Technology (Beijing) Co., Ltd.). The experimental procedure was as follows: BC of a precisely weighed sample was loaded into a dedicated sample tube of known weight. The tube was then connected to the instrument's degassing station. Under a flowing inert gas (high-purity N_2) environment, the sample was subjected to a thermal treatment to ensure the removal of deeply adsorbed species. Following this, the sample tube was mounted onto the instrument's analysis port and immersed in a dewar flask containing liquid nitrogen to maintain a constant temperature of 77.3 K. The instrument introduced nitrogen gas into the sample

tube in a controlled, stepwise manner, precisely measuring the volume of gas adsorbed by the sample at each equilibrium pressure point. After reaching the maximum pressure, a stepwise reduction in pressure was performed to measure the desorption branch, generating a complete adsorption-desorption hysteresis loop. The samples were degassed at 150 °C for 500 min prior to analysis.

The surface functional groups of the BC were analyzed using a Thermo Scientific Nicolet iS10 Fourier-transform infrared (FTIR) spectrometer equipped with an optimized mid-IR KBr beamsplitter covering a spectral range of 350 to 7800 cm^{-1}. The operational protocol was as follows: The FTIR spectrometer and computer were powered on and allowed to warm up and stabilize for at least 30 min. The instrument's internal compartment was purged with dry nitrogen. Subsequently, approximately 1-2 mg of the dried BC's sample was thoroughly mixed and ground with 100-200 mg of dried potassium bromide (KBr) in an agate mortar until a very fine and homogeneous mixture was obtained. This mixture was then transferred into a pellet die and subjected to a pressure of approximately 8-10 MPa using a hydraulic press for 1-2 min to form a transparent or semi-transparent pellet. For background correction, a pure KBr pellet was first placed in the sample holder, and a background spectrum was scanned and stored. Finally, the prepared BC/KBr pellet was placed in the sample compartment for spectral acquisition.

2.2. Experimental apparatus and procedure

2.2.1. Experimental apparatus

A schematic diagram of the experimental apparatus for hydrate-based hydrogen storage was shown in Fig. 1. The system comprised a high-pressure autoclave, a gas cylinder, a gas booster pump, a low-temperature thermostatic bath, a data acquisition system (DAQ), and a computer. The core component of the hydrate hydrogen storage apparatus was a high-pressure autoclave constructed from 316 L stainless steel, with an effective volume of 312 mL and a maximum working pressure of 40 MPa. A low-temperature thermostatic bath (Model THD-3030, Ningbo Tianheng Instrument Factory, China; temperature stability ±0.1 K) was employed to control the experimental temperature. A PT-100 temperature sensor (Shanghai Yijia Electric Heating Co., Ltd., China; accuracy ±0.1 K) and a pressure transducer (Guangzhou Sennai Instrument Co., Ltd., China; accuracy ±0.01 MPa) were connected to the top flange of the autoclave to monitor temperature and pressure throughout the experiments. Temperature and pressure data were recorded using a data acquisition system (Agilent Technologies, Inc.) interfaced with a computer.

2.2.2. Procedure and Raman spectroscopy measurements

To facilitate solution dispersion within the BC pore network and mitigate hydrogen mass transfer resistance, IP was implemented, involving the removal of excess solution external to the BC matrix. Initially, BC particles were rinsed with deionized water to eliminate surface contaminants, with rinsing repeated until effluent clarity was achieved; subsequently, the rinsed BC was dehydrated in a drying oven at 75 °C.

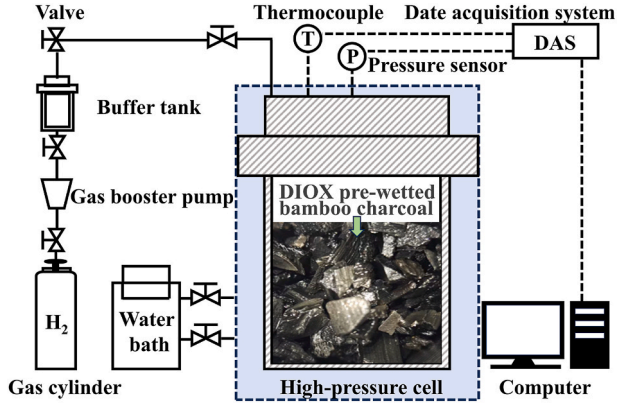

Fig. 1. Schematic diagram of the experimental setup for hydrate-based hydrogen storage.

Precisely 50 g of dried BC was rapidly weighed into a 250 mL wide-mouth bottle, followed by addition of a stoichiometric DIOX solution (5.56 mol%); the bottle was then sealed for immersion. Concurrently, the circulating water bath was activated, reactor gas tightness was verified, and the reactor temperature was stabilized at the target experimental value. Following immersion, residual solution in the bottle was decanted; the mass of DIOX solution absorbed by the BC was determined gravimetrically. The pre-wetted BC was then transferred into the reactor, which was immediately positioned within a water bath pre-cooled to the setpoint temperature. The data acquisition system was initiated to record reactor temperature and pressure at 10-s intervals. The reactor was evacuated using a vacuum pump, then pressurized with H_2 to 1~1.5 MPa above the target experimental pressure. Hydrogen was promptly replenished as pressure decreased toward the target value; hydrate formation was considered complete upon pressure stabilization, defined by a rate of pressure change ($\Delta P/\Delta t$) below 0.01 MPa h^{-1}.

In the IP, each pore within the BC matrix effectively functions as a micro-reactor, significantly minimizing heat and mass transfer resistances and thereby promoting the prospect of high-density hydrogen hydrate storage, as conceptually depicted in Fig. 2. The second-stage hydrogen injection strategy involved promptly replenishing hydrogen to the designated pressure whenever the system pressure falls below this target, thereby increasing the hydrogen concentration gradient. As the hydrogen injection process induced a transient temperature rise, subsequent rapid cooling coupled with ongoing hydrogen consumption by hydrate formation caused a sharp pressure decline. To ensure the system pressure remains consistently above the target value after cooling, the initial pressurization consistently exceeded the target pressure by 1~1.5 MPa.

The hydrate samples within the BC's channels were analyzed using a confocal micro-laser Raman spectrometer (Model RTSmini-301MS532-SMS, Beijing Zolix Instruments Co., Ltd., https://www.zolix.com.cn/). Prior to analysis, the BC was sectioned under a liquid nitrogen atmosphere to preserve the hydrate. The sample was then placed on the microscope stage, and the region of interest was located and precisely focused using a 50 × objective. Spectra were acquired with a laser wavelength of 532 nm, a power of 10 mW, over a wavenumber range of 200–4200 cm^{-1}, and an integration time of 2 s per scan. Data collection commenced after parameter configuration, allowing for real-time monitoring of the spectral signal. This analysis aimed to confirm the formation and identity of the DIOX–H_2 hydrate within the confined pores.

2.3. Data processing

During hydrate formation, the H_2 consumption at time "*i*"is defined as the difference between the initial amount of H_2 (n_0) in the high-pressure reactor at time "0" and the amount of H_2 (n_i) present at time "*i*". This H_2 consumption can be mathematically expressed by equation (1). For experiments involving second-stage hydrogen injection, the total hydrogen consumption ($\triangle n_{H_2}$) is determined by the cumulative summation of the hydrogen consumed during each distinct replenishment stage.

$$\Delta n_{H_2} = (n_0 - n_i) = \frac{P_0 V}{Z_0 R T_0} - \frac{P_i V}{Z_i R T_i} \quad (1)$$

Where "*n*" is the number of moles of hydrogen (mol); V, $V_{reactor}$, $V_{solution}$, and $V_{dead\ volume\ of\ BC}$ represent the gas phase volume (m^3), reactor volume (m^3), solution volume (m^3), and dead volume of BC (m^3) in the reactor,

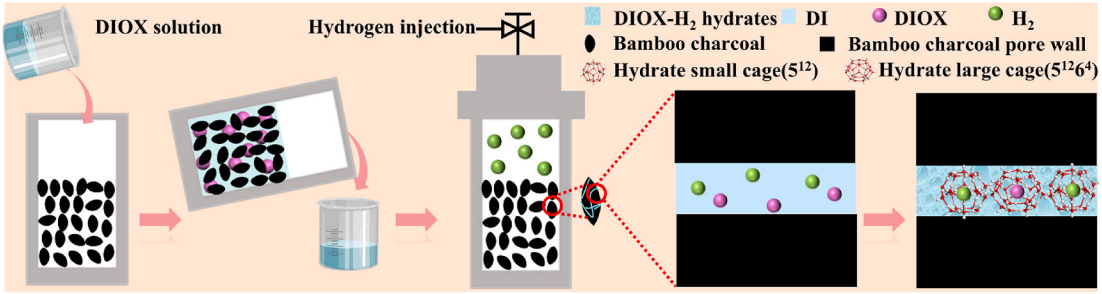

Fig. 2. Schematic diagram of hydrogen storage using hydrate formed within BC channels.

respectively; R is the universal gas constant (8.314 J mol^{-1} K^{-1}); P and T denote the instantaneous pressure (Pa) and temperature (K) within the reactor; and Z is the compressibility factor, calculated using the Redlich-Kwong equation. The subscripts "0" and "i" correspond to the start of the experiment and an arbitrary time (h) during the reaction process, respectively. The gas phase volume (V_g) is determined by equation (2).

$$V = V_{reactor} - V_{solution} - V_{dead\ volume\ of\ bamboo\ charcoal} \tag{2}$$

The growth rate (r, mmol/min) of the DIOX-H_2 mixed hydrates formation process can be determined by equations (3) and (4).

$$r = \frac{(n_{H_2})_i - (n_{H_2})_{i+10}}{\Delta t} \tag{3}$$

$$\Delta t = t_{i+10} - t_i \tag{4}$$

Where "r" represents the growth rate (mmol/min), and "n" is the number of moles of hydrogen (mol). The subscripts "i" and "$i+10$" denote the time points"i" and "$i+10$" during the experimental reaction process, respectively. Due to the finite sampling interval of the data acquisition system, the rates calculated in this work are not instantaneous rates but represent the average hydrogen storage rate over the sampling interval.

The H_2 storage density in the hydrate, defined as the mass of hydrogen consumed divided by the initial mass of water (wt%), is given by equation (5). Here, m_{H_2O} represents the initial mass of water (g) within

$$wt\% = \frac{\Delta n_{H_2} \times 2}{m_{H_2O}} \times 100 \tag{5}$$

the BC. It is assumed that the THF concentration in the pore water of the BC after pre-wetted via immersion remains consistent with the initial prepared THF solution. Furthermore, the hydrogen storage rate (wt%/h) is obtained by dividing the hydrogen storage density per unit mass by the corresponding time required.

To further demonstrate the benefit of the second-stage hydrogen injection method for enhancing hydrate-based hydrogen storage density, the percentage increase in hydrogen storage capacity achieved in each stage of this method can be determined by equation (6).

$$\frac{\Delta n_{H_2,k+1} - \Delta n_{H_2,k}}{\Delta n_{H_2,1}} \times 100 \tag{6}$$

Where $\Delta n_{H_2,1}$ denotes the hydrogen consumption (mol) during the first gas introduction stage, $\Delta n_{H_2,k}$ represents the hydrogen consumption (mol) during the k-th hydrogen injection stage, and $\Delta n_{H_2,k+1}$ signifies the hydrogen consumption (mol) during the (k+1)-th hydrogen injection stage, where k is a positive integer greater than or equal to 1 ($k \geq 1$).

3. Results and discussion

3.1. Hydrate-based hydrogen storage enhanced by pre-wetted BC

Prior studies promoting hydrate-based hydrogen storage with porous materials typically required direct mixing with promoter solution before H_2 exposure [38], leaving excess unbound solution between particles. This configuration impedes hydrogen transfer as hydrates form at interfaces. To overcome this, this work introduced immersion-pre-wetted (IP): DIOX solution was dispersed within BC pores via immersion, with excess solution drained. This eliminated free liquid between BC particles, ensuring all pore water participated in reaction and achieving high hydration efficiency.

Three systems were compared at 274.15 K/18 MPa under static conditions: (i) pure DIOX solution (no BC), (ii) direct-addition (DA) of BC + DIOX, and (iii) immersion-pre-wetted BC, all using single-stage H_2 injection initiated at injection completion. Fig. 3(a) shown pressure drops of 0.26 MPa (pure), 0.85 MPa (DA), and 1.28 MPa (IP), indicating progressively higher H_2 consumption with IP. Compared to pure dioxolane solution, the DA and IP methods resulted in significantly smaller temperature fluctuations during hydrogen hydrate formation, indicating that bamboo charcoal can effectively remove the heat of formation. Correspondingly, Fig. 3(b) revealed DA enhanced storage density 22-fold (from 0.012 wt% to 0.275 wt%) versus pure system, achieving 17.26 mmol/min peak formation rate. This enhancement stemmed from BC dispersing solution within pores—expanding gas-liquid interfaces and accelerating heat dissipation—Fig. 3(a) ultimately validating BC's critical role in advancing hydrate-based hydrogen storage.

Then, compared to the DA for hydrate-based hydrogen storage, it was found that the IP (E2) significantly enhanced the hydrogen storage density in DIOX-H_2 hydrates, achieving a 101% increase. The hydrogen storage density using the IP method reached 0.553 wt%, representing a 101% improvement over the DA method.

The IP method of Fig. 3(b) achieved 0.455 wt% storage density at 0.5 h with a rate of 0.910 wt%/h, surpassing the DA method's final density. It required only 0.09 h to reach DA's equivalent density—a 98.5% time reduction. Both DA and IP systems showed gradual density increases without induction periods, attributable to BC providing nucleation sites for rapid hydrate initiation. This contrasts sharply with Kong et al.'s [20] 7.39 h induction period in BC-free DIOX-H_2 systems. By eliminating induction delays entirely, IP significantly accelerates the entire storage process, establishing a practical pathway for efficient hydrate-based hydrogen storage.

Subsequently, the hydrogen adsorption capacity of BC was analyzed. Fig. 4 displayed the amount of hydrogen adsorbed by BC, revealing that the final hydrogen consumption within BC was minimal. This indicated that BC did not adsorb hydrogen, confirming that the subsequent hydrogen storage capacity achieved via the IP is entirely attributable to hydrogen storage within the DIOX-H_2 hydrates.

The IP method's superior storage density stems primarily from eliminating unhydrated free water between BC particles, thereby avoiding mass transfer barriers that impede DIOX-H_2 hydrate formation. Crucially, in DA systems, hydrates preferentially form in BC interstices, obstructing late-stage hydrogen diffusion and limiting final density. Conversely, IP confines hydrate growth within BC pores—eliminating hydrogen transfer limitations and enabling significantly higher storage density through pore-level confinement.

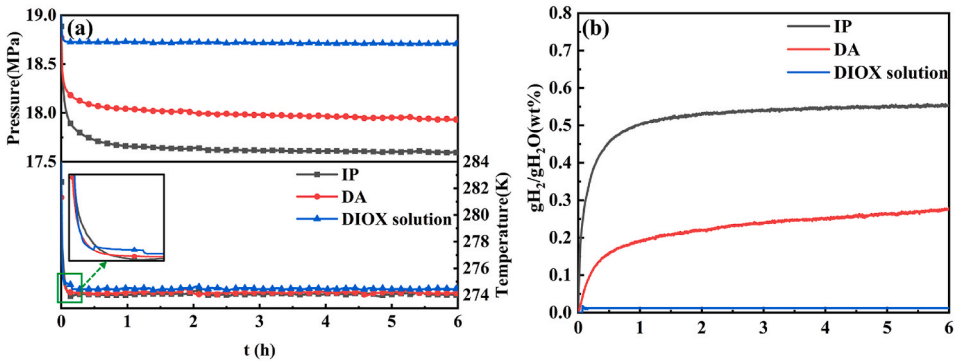

Fig. 3. Hydrate formation process for DIOX solution without BC, AD and IP, 274.15 K and 18 MPa. (a) The curve of temperature and pressure of hydrate formation; (b) Hydrogen storage capacity.

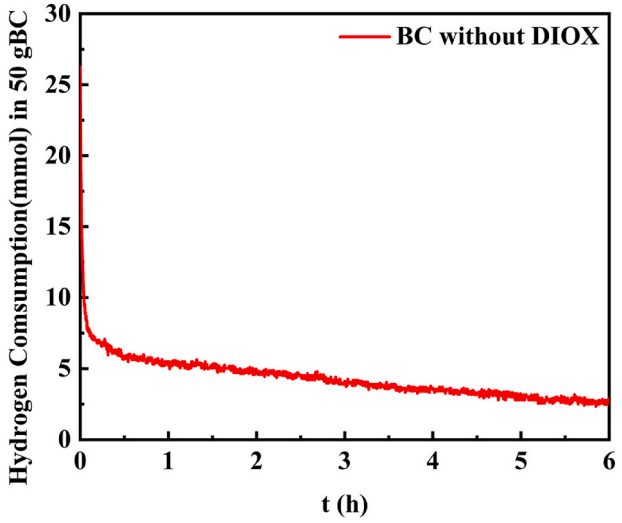

Fig. 4. Hydrogen adsorption capacity of 50 g BC in 274.15 K and 18 MPa.

3.2. Second-stage hydrogen injection enhancing hydrogen storage in DIOX hydrate

Fig. 3(a) revealed a gradual pressure decline after 0.5 h in single-stage H_2 injection systems, indicating insufficient driving force ($\Delta P = P_{exp} - P_{eq}$) that sharply reduced hydrate storage density growth. To overcome this limitation and enhance storage density, this work implemented second-stage hydrogen injection to replenish H_2 when driving force diminished, effectively boosting storage capacity as detailed in Section 2.3.

Second-stage H_2 injection significantly enhanced hydrate storage density versus single-stage injection. Fig. 5(a) and (b) compared temperature-pressure profiles and density evolution for both methods: Single-stage injection (E3) showed rapid pressure drop (<18 MPa at 0.25 h) with subsequent stabilization, while density growth sharply decelerated after 0.5 h (Fig. 5(b)) due to insufficient driving force—yielding only 0.553 wt% after 6 h. This limitation underscores the critical advantage of staged injection for sustaining high-density storage.

The second-stage H_2 injection method promptly replenished hydrogen as pressure neared the critical 18 MPa threshold at 0.25 h, sustaining pressure >18 MPa post-hydration. Consequently, storage capacity surged rapidly after second-stage hydrogen injection, achieving 0.724 wt% final density—a 30.9% increase over single-stage methods—with peak hydrate growth reaching 53.64 mmol/min. These results confirm staged injection's critical role in enhancing hydrate storage density through dynamic driving force maintenance.

In summary, the second-stage hydrogen injection enhances the mid-to-late stage driving force in DIOX-H_2 mixed hydrate formation by replenishing hydrogen once pressure fallen below 18 MPa, significantly increasing the final hydrogen storage density.

3.3. Pressure and temperature on hydrogen storage capacity in DIOX hydrate

3.3.1. Pressure on hydrogen storage capacity in DIOX hydrate

Pressure exerts the most dominant effect on gas solubility; increasing solubility is critical for accelerating hydrate growth [44]. During DIOX-H_2 mixed hydrate hydrogen storage using single-stage injection, the gradual pressure decrease reduces the formation driving force, limiting hydrogen storage density enhancement. Thus, this study employed the second-stage injection method (Section 3.2) to augment the late-stage driving force under varying pressures. Since experimental

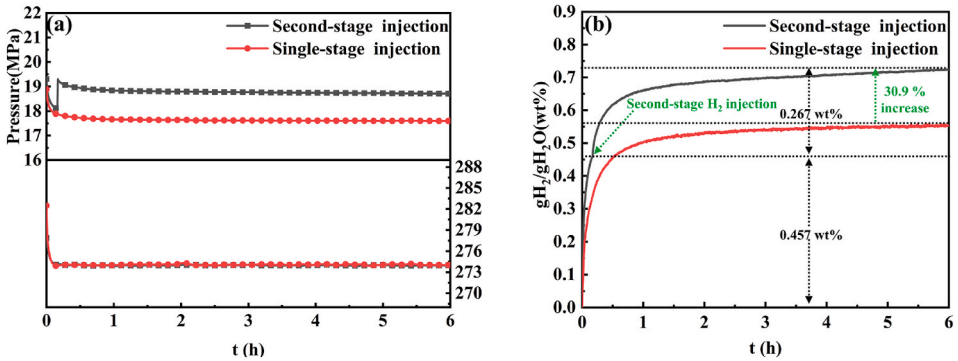

Fig. 5. Hydrogen storage capacity of DIOX-H_2 hydrates with different injection methods via IP, 274.15 K and 18 MPa. (a) The curve of temperature and pressure of hydrate formation; (b) Storage density.

pressure critically influences this driving force and, consequently, the ultimate storage density, evaluating the second-stage method's efficacy across different pressures is crucial.

Results shown that hydrogen storage density in DIOX-H_2 mixed hydrates increases monotonically with pressure. Fig. 6(a) depicted the temperature and pressure profiles during hydrogen storage at 274.15 K under varying initial pressures, revealing a pressure drop below the setpoint within 0.5 h, prompting hydrogen replenishment to maintain reactor pressure and enhance the driving force for subsequent hydrate formation. As shown in Fig. 6(b) and summarized for groups E5~E7 (Table 1), storage density gradually rose at 274.15 K with elevated initial pressure, reaching 0.542 wt% after 6 h. The final density at 20 MPa exceeded that at 18 MPa and 15 MPa by 16.06% and 35.50%, respectively, directly attributable to the stronger driving force during hydrate formation at higher pressures.

To identify the primary hydrogen consumption period during hydrate-based storage, Fig. 6(b) illustrated hydrogen storage density distribution in DIOX-H_2 mixed hydrates across distinct intervals: 0~1 h, 1~3 h, and 3~6 h. Analysis revealed that most hydrate formation and hydrogen storage occurred within the first hour post-injection. During the critical 0~1 h interval, hydrogen storage densities at 15, 18, and 20 MPa reached 84.75%, 84.80%, and 71.03% of final values, respectively, confirming predominant storage occurred within the first hour post-injection. Although minor density increased continued beyond 1 h, hydrogen consumption plateaued gradually. This pattern arisen because water rapidly converts to DIOX-H_2 hydrates in the initial window, with DIOX preferentially occupying large cages ($5^{12}6^4$) and leaving abundant vacant small cages (5^{12}) for efficient hydrogen trapping. Subsequently, diminished small-cage availability—combined with diffusion hindrance from large-cage DIOX molecules as reported by Hasegawa et al. [45]—significantly slow storage kinetics.

Fig. 6(c) illustrated hydrogen replenishment's impact on clathrate hydrate storage, comparing single-stage versus second-stage injection across 15~20 MPa experiments. Results confirmed second-stage hydrogen injection significantly enhanced storage density: initial storage (pre-replenishment) measured 0.272, 0.304, and 0.319 wt% at 15/18/20 MPa, while second-stage injection added 0.110, 0.144, and 0.162 wt%, respectively. This yielded 47.00%, 43.71%, and 78.40% density increases—demonstrating that augmented mid-late stage driving forces facilitate hydrogen occupancy in DIOX-H_2 hydrates small cages (5^{12}), thereby boosting overall storage.

Fig. 6(d) shown t_{90} (time to reach 90% final storage density), revealing longer t_{90} correlated with higher storage densities. Values measured 78.33, 78.17, and 169.50 min at 15/18/20 MPa, respectively. This occurred because at lower pressure (15 MPa, $\Delta P = 5.8$ MPa) [46], limited driving force rapidly saturates hydrate storage, shortening t_{90}. Conversely, higher final densities require sustained substantial driving forces during later stages—achieved at elevated pressures—thus extending formation time and t_{90}.

3.3.2. *Temperature on hydrogen storage capacity in DIOX hydrate*

Lower temperatures provide greater driving force for hydrogen storage in clathrate hydrates but risk ice formation. Conversely, higher temperatures increase hydrogen activity and molecular motion, potentially accelerating hydrate kinetics. However, as shown by the DIOX-H_2 hydrates phase equilibrium curve, excessively high temperatures significantly reduce the driving force. Thus, identifying an optimal temperature range is crucial for efficient clathrate hydrate hydrogen storage.

Fig. 7(a) illustrated hydrogen storage density evolution over time at these temperatures. Results demonstrated that at constant pressure, storage density increases with decreasing temperature. Remarkably, 0.726 wt% was achieved at 272.15 K and 18 MPa, surpassing the highest reported DIOX hydrate storage density by 0.299 wt%—representing 170% of the previous value [29].

Final hydrogen storage densities measured 0.726 wt% at 272.15 K, 0.542 wt% at 274.15 K (25.34% decrease), and 0.470 wt% at 276.15 K (35.26% decrease). With corresponding initial driving forces of 9 MPa (274.15 K) and 3 MPa (276.15 K) [46], these findings indicate the storage density reduction with rising temperature is primarily attributable to diminishing driving forces—becoming insufficient for effective hydrogen storage.

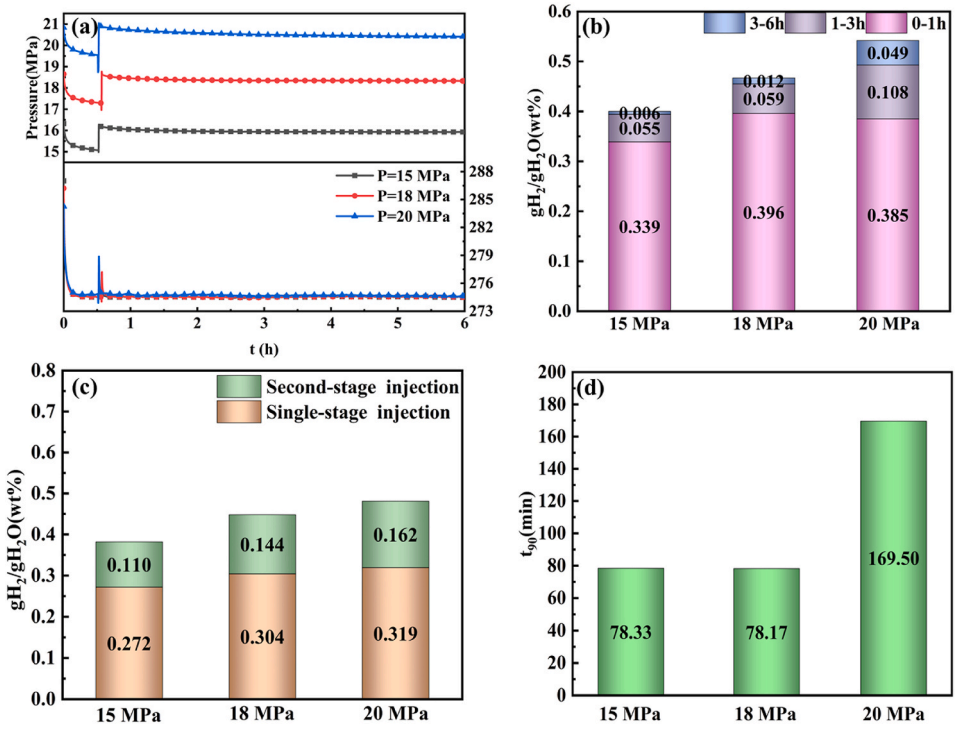

Fig. 6. Hydrogen storage capacity of DIOX-H_2 hydrates under different pressures, 274.15 K.(a) The curve of temperature and pressure of hydrate formation; (b) Hydrogen storage density; (c) Storage density distribution in different gas injection stages; (d) The time of the maximum gas uptake of 90% (t_{90}).

Table 1
Hydrogen storage performance parameters for IP and second-stage hydrogen injection (static).

Case	Temperature (K)	Presssure (MPa)	Single-stage hydrogen consumption (mmol)	Secong-stage hydrogen consumption (mmol)	Final hydrogen consumption(mmol)	Hydrogen storage capacity(gH_2/gH_2O,wt%)	r_{max}($mmolH_2$/min)
E1	274.15	18	29.08	-	29.08	0.275	5.50
E2	274.15	18	59.60	-	59.60	0.553	17.26
E3	274.15	18	59.60	-	59.60	0.553	17.26
E4	274.15	18	74.75	43.69	118.44	0.724	53.64
E5	274.15	15	43.81	20.59	64.40	0.400	9.55
E6	274.15	18	46.58	20.36	66.94	0.467	41.06
E7	274.15	20	45.37	35.57	80.94	0.542	11.59
E8	272.15	18	33.35	43.95	77.30	0.726	55.72
E9	274.15	18	41.75	21.75	63.50	0.574	34.23
E10	276.15	18	30.41	20.30	50.17	0.470	13.13

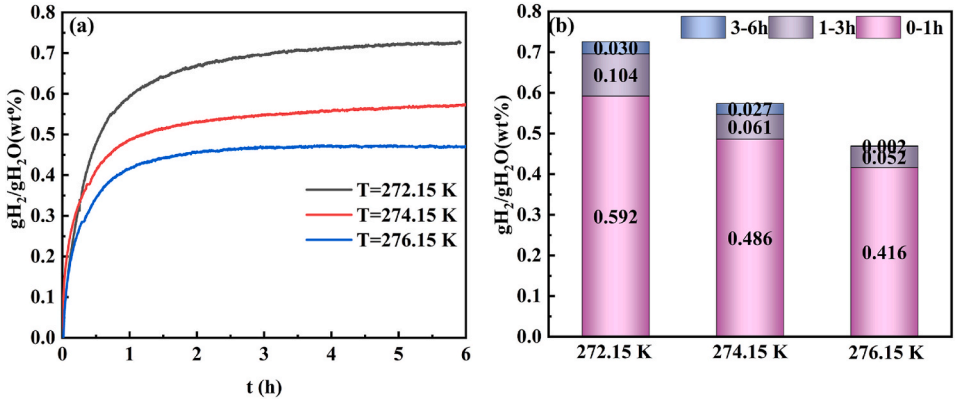

Fig. 7. Hydrogen storage capacity in DIOX-H_2 hydrate under different temperatures, 18 MPa. (a) DIOX hydrate hydrogen storage capacity; (b) hydrogen storage density during different time periods.

Understanding the primary hydrogen consumption phase was essential for shortening the overall storage time. Fig. 7(b) presented the distribution of hydrogen storage density across distinct time intervals, 0~1 h, 1~3 h and 3~6 h. The results reveal that lower temperatures correlate with a higher proportion of storage occurring within the first hour (0~1 h), confirming this period as the dominant phase for hydrogen consumption. Specifically, storage densities within 0~1 h reached 0.592 wt%, 0.486 wt%, and 0.416 wt% at 272.15 K, 274.15 K, and 276.15 K, respectively, constituting 81.54%, 89.67%, and 88.51% of the respective final storage densities. Furthermore, a particularly striking observation was that at 272.15 K, a storage density of 0.480 wt % was achieved within merely 0.5 h. This value already exceeded the storage density of 0.427 wt% reported in the literature for DIOX-H_2 mixed hydrates after 16 h of formation [29], representing a reduction in time to achieve equivalent storage by 97%. This highlights the dual advantage of the low-temperature condition, exceptionally high ultimate storage density coupled with remarkably rapid storage kinetics.

In summary, the driving force emerges as the paramount factor governing hydrogen storage density in clathrate hydrates. The observed decrease in hydrogen storage density with increasing temperature is a direct consequence of the insufficient driving force available under warmer conditions.

3.4. The mechanism of BC in enhancing hydrogen storage

As established in Section 3.1, BC played a critical role in significantly accelerating the hydrogen storage kinetics and enhancing the ultimate storage density within DIOX-H_2 mixed hydrates. Therefore, a detailed analysis of the underlying mechanisms by which BC promoted DIOX-H_2 mixed hydrates formation was essential.

3.4.1. FTIR analysis of BC

Understanding the surface functional groups of BC is crucial for analyzing its role in enhancing hydrate-based hydrogen storage. Fig. 8 displays the FTIR spectrum of the BC. The broad peak observed at approximately 3200 cm^{-1} is characteristic of O–H stretching vibrations. The sharp, narrow peak at around 1700 cm^{-1} is attributed to the C═O stretching vibration, while the pronounced peak at approximately 1230 cm^{-1} corresponds to C–O stretching [47]. Based on this analysis, the presence of –OH, –COOH, and –C═O functional groups on the surface of the BC is confirmed. These groups render the BC hydrophilic, enabling it to effectively disperse and immobilize water and THF molecules.

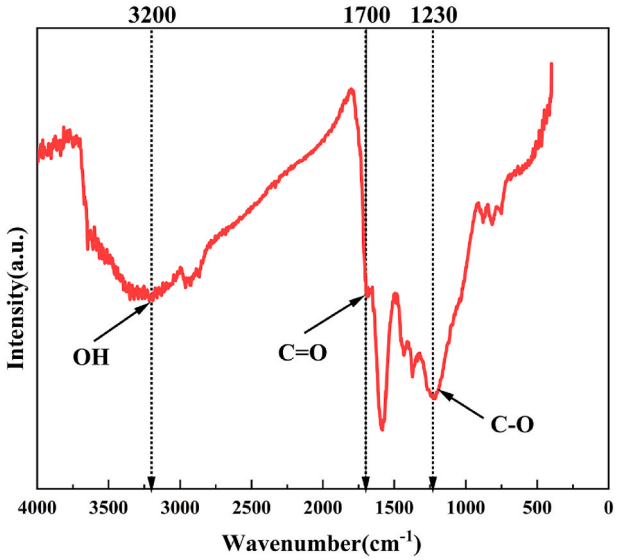

Fig. 8. The FTIR spectrum of the BC.

3.4.2. Analysis of cyclability and stability for BC-enhanced hydrogen storage

The cyclic hydrogen storage capacity of the DIOX pre-wetted system was investigated. As shown in Fig. S1(a), during the first hydrogen storage cycle at 274.15 K and 20 MPa, the system achieved a storage density of 0.600 wt%. Subsequently, the temperature was increased to 298.15 K to completely decompose the DIOX-H_2 hydrate, followed by cooling back to 274.15 K to reform DIOX-H_2 hydrate. However, as shown in Fig. S1(b), the hydrogen storage density decreased to 0.273 wt % in the second cycle, representing a 54.5% reduction compared to the first cycle. This indicates relatively poor recyclability, which is a key limitation of the present study. The morphological changes of the BC before and after hydrogen storage are presented in Fig. S2. Significant fragmentation of the BC is observed, compromising its structural integrity. The resulting BC's powder likely blocks the pores or causes particles to agglomerate, thereby increasing mass transfer resistance for hydrogen. This structural degradation is likely a primary reason for the poor cyclic performance observed in the BC system for hydrate-based hydrogen storage.

To investigate the underlying cause of the poor cyclic hydrogen storage performance in the BC system, changes in the pore size distribution of the BC before and after hydrogen storage were analyzed. Fig. S3 displays the N_2 adsorption-desorption isotherm and pore size distribution of the BC prior to hydrogen storage. The isotherm exhibits a type II pattern, which is commonly observed in porous media with pore diameters exceeding 20 nm. The pore size distribution of the BC prior to hydrogen storage is presented in Table S1. Micropores, mesopores, and macropores accounted for 12.75 %, 86.60 %, and 0.65 % of the total pore volume, respectively, indicating a predominance of mesopores. The relatively larger size of mesopores is favorable for the dispersion and accommodation of the liquid phase within the channels. Fig. S4 presents the N_2 adsorption-desorption isotherm and pore size distribution of the BC after hydrogen storage. The isotherm exhibits a type I pattern, indicating the predominant presence of micropores and mesopores in the BC, with pore sizes primarily distributed below 10 nm. In contrast, the pore size distribution after hydrogen storage cycles (Table S2) shows a significant shift: micropores, mesopores, and macropores accounted for 69.98 %, 30.02 %, and 0.00 %, respectively. This demonstrates a predominance of micropores post-cycling, with the mesopore volume fraction drastically decreasing by 56.58 % and macropores completely disappearing. These results indicate poor structural stability of the BC during cyclic hydrogen storage operations. The solution, initially uniformly dispersed within the intact pore network (forming an array of "micro-reactors"), loses its ordered dispersion state as the pore structure collapses, leading to a substantial reduction in the effective gas-liquid reaction interface. The fragmentation of the BC generated a substantial amount of fine powder. This BC's powder can be agglomerated by the liquid solution, leading to pore blockage and increased mass transfer resistance for hydrogen. This structural degradation and resulting increased diffusion barriers are likely the primary reasons for the deteriorated cyclic hydrogen storage capacity.

Understanding the surface morphology of BC and the structural evolution of its pore channels before and after the hydrogen storage process was key to elucidating these mechanisms. Fig. 9(a) displayed the morphology of dried BC particles, exhibiting dimensions ranging from 6 to 12 mm. Fig. 9(b) presented a Scanning Electron Microscopy (SEM) image of BC prior to its use in DIOX-H_2 mixed hydrates formation. The image revealed that BC possesses an abundant, honeycomb-like pore structure with diverse pore sizes. The inter-wall spacing was approximately 1~5 μm, with primary pore channels measuring 5~20 μm. Additionally, a minor fraction of smaller micropores within the 1~5 μm range was observed.

According to Roodbari et al. [48], the formation pressure of DIOX-H_2 hydrates within porous media remained comparable to the equilibrium pressure in pure water when the pore diameter exceeded 100 nm. Consequently, utilizing BC as a porous medium for hydrogen storage did not significantly alter the phase equilibrium conditions for DIOX-H_2 mixed hydrates. Thus, the phase equilibrium behavior in this system aligned with that of bulk DIOX-H_2 solution.

Furthermore, the observed rapid initial increase in hydrogen storage density, reaching near-stable levels within 0~1 h, was primarily attributed to the confinement of hydrate formation exclusively within

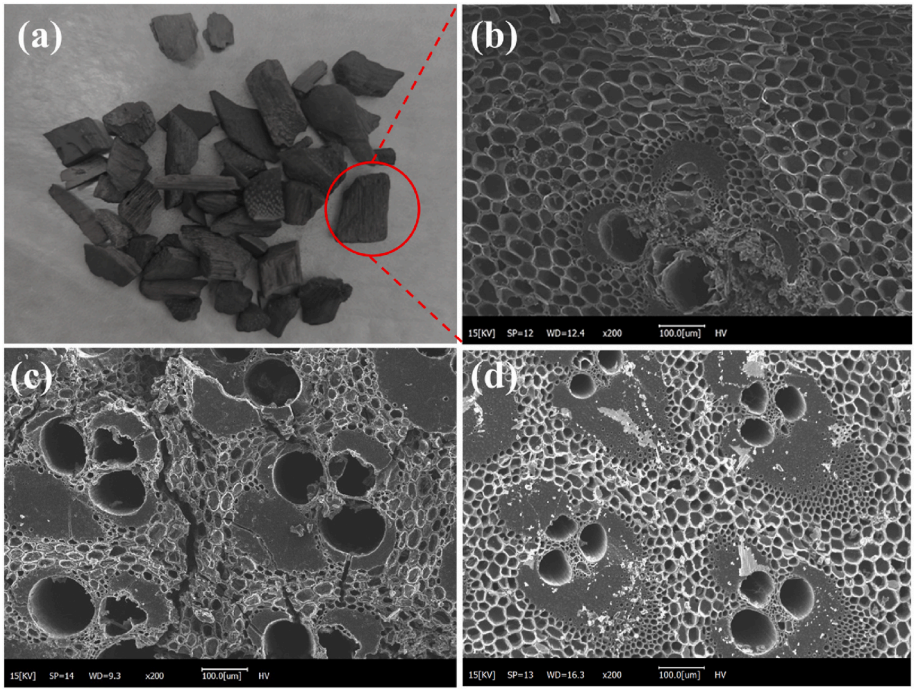

Fig. 9. Morphological evolution of BC during DIOX hydrate hydrogen storage. (a) Pristine BC microstructure; (b) BC morphology before DIOX hydrate-based hydrogen storage; (c) BC morphology after DIOX hydrate-based hydrogen storage with second-stage hydrogen injection, 274.15 K and 18 MPa; (d) Bulk deionized water pre-wetted BC after second-stage hydrogen injection, 274.15 K and 18 MPa.

the internal pore channels of BC. The efficacy of BC stemmed from its unique properties, its abundant micron-scale pore network, intrinsic surface roughness and favorable thermal conductivity. These properties collectively facilitate (1) the effective dispersion of the DIOX solution, (2) a substantial increase in the gas-liquid contact area, (3) the provision of abundant nucleation sites for clathrate hydrate, and (4) the efficient dissipation of the heat generated during hydrate formation. When combined with the second-stage hydrogen injection method, which maintained a sufficient driving force throughout the storage process, this approach enabled highly efficient hydrogen storage within DIOX-H_2 mixed hydrates.

Fig. 9(c) presented the SEM micrograph of BC after the DIOX-H_2 mixed hydrates hydrogen storage reaction. The image revealed partial fracturing on the BC surface and fractured pore channels, predominantly affecting micropores larger than 10 μm. Additionally, the BC exhibited reduced rigidity and increased brittleness. To elucidate the cause of this pore channel fracturing, Fig. 9(d) shown the morphology of BC pre-wetted with bulk deionized water after hydrogen storage. In this case, the pore structure of BC remained intact, closely resembling the morphology of dried BC. A direct comparison between Fig. 9(c) and (d) indicated that the fracturing of BC was attributed to the volumetric expansion associated with DIOX-H_2 hydrates growth within the pore channels. This mechanism was schematically illustrated in Fig. 10, depicting how hydrate formation and expansion within the pores fracture the BC structure. This partial fragmentation of the BC pore network further enhanced the contact area between the DIOX solution and hydrogen. This increased interfacial area is a key factor contributing to the consistently rapid hydrogen storage rate observed within the initial 0.5h in this work.

In summary, the results indicate that the volumetric expansion during hydrate formation leads to extensive fragmentation of mesopores and macropores. Following pore fragmentation, the specific surface area of micropores increased remarkably from 0.1838 m^2/g to 162.1309 m^2/g in Tables S1 and S2. Consequently, the breakdown of BC further enhances the gas-liquid contact area, intensifies the mass transfer process of hydrogen, and improves the conversion rate from water to hydrate. This contributes to the observed faster hydrogen storage kinetics and higher storage density. Furthermore, as shown in Fig. 4, BC does not exhibit hydrogen adsorption capacity; thus, the presented system is not a combination of adsorption-based and hydrate-based hydrogen storage. The hydrogen storage capacity reported in this work is entirely attributed to hydrogen trapping within DIOX-H_2 hydrate. The dispersion of the solution via IP plays a crucial role in enhancing the hydrogen storage capacity of the DIOX-H_2 hydrate.

3.4.3. *Morphology of DIOX–H_2 hydrate and hydrogen occupation behavior in DIOX solution of BC's pores*

Understanding the growth behavior of DIOX-H_2 hydrate within the BC's pores is crucial. Fig. 11(a) presents a cross-sectional view of the BC, revealing a grid-like distribution of pores with interconnected channels between them. Each pore channel functions similarly to a "micro-reactor", which can significantly increase the gas-liquid contact area while markedly reducing hydrogen mass transfer resistance. The DIOX solution can be uniformly distributed within the BC' pores, as detailed in Fig. S5. The bright areas represent the DIOX solution. Subsequently, to clarify the growth morphology and state of DIOX-H_2 hydrate within the BC's channels, observations were conducted using microscopy at 50 × magnification under low-temperature conditions (approximately −153 K). As shown in Fig. 11(b), the white thin layer corresponds to the DIOX-H_2 hydrate. It can be seen that the hydrate grows in a film-like form, uniformly dispersed within each pore channel of the BC. The resulting DIOX-H_2 hydrate is on the micrometer scale, achieving the initial objective of utilizing the BC's pores as "micro-reactors" to enhance hydrogen storage performance.

To clarify the cage occupancy of hydrogen in DIOX–H_2 hydrate within the BC's pores, Raman spectroscopy was employed to analyze the characteristic peak shifts of the hydrate confined in the channels. Fig. 12 displays the full Raman spectrum of the 5.56 mol% DIOX-H_2 hydrate sample. Two distinct characteristic peaks were observed at 941.4 and 960.2 cm^{-1}, which are attributed to the C–C and C–O stretching vibrations of the DIOX molecule, respectively. Three characteristic peaks were detected at 2760.0, 2850.0, and 2885.2 cm^{-1}, indicating the inherent C–H stretching vibrations of the DIOX molecule occupying the large ($5^{12}6^4$) cages of the hydrate [28,46]. Additionally, the characteristic peak at 3106.1 cm^{-1} corresponds to the O–H stretching vibration of water molecules in the hydrate framework. Finally, a pronounced H_2 peak was observed at 4130.7 cm^{-1}, attributed to single hydrogen molecules occupying the 5^{12} small cages of the hydrate [47,49,50] and no evidence was found for double hydrogen occupation of the 5^{12} cages. In conclusion, the formation of DIOX–H_2 hydrate within the BC's pores is conclusively demonstrated.

In summary, the inherently abundant and interconnected pore channels of BC effectively disperse the solution, thereby enhancing the mass transfer of hydrogen. The growth process of DIOX–H_2 hydrate subsequently leads to the fragmentation of these pore channels, which exposes the internal solution to direct contact with hydrogen. This gradual increase in the contact area between hydrogen and the DIOX solution during hydrate growth macroscopically manifests as an initially very rapid hydrogen storage rate and a significantly improved final storage density. The formation of DIOX–H_2 hydrate within the pores is conclusively demonstrated by Raman spectroscopy. Thus, future efforts should therefore focus on enhancing BC's mechanical strength or identifying alternative porous materials with similar beneficial properties (e.g., favorable pore structure, thermal conductivity, surface roughness) but superior strength. Preventing hydrate-induced pore fracturing is essential for improving cyclability of the IP hydrogen storage method.

3.5. *Hydrogen storage capacity of the IP method*

To demonstrate the significant efficacy of this work in advancing hydrogen storage technology in DIOX-H_2 hydrates, a comparative analysis was conducted against existing literature. As summarized in Table 2, this work was benchmarked against prior studies concerning hydrogen storage density, hydrogen uptake rate, and hydrate formation quantity. The reported hydrogen storage densities from the literature were normalized to the ratio of hydrogen consumed to the mass of water

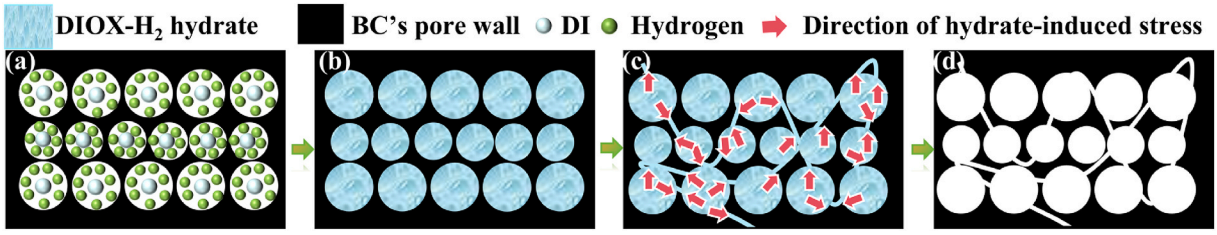

Fig. 10. The mechanism of enhancing DIOX-H_2 hydrate formation with BC. (a) Second-stage hydrogen injection; (b)Hydrate formation; (c) Volume increase during hydrate growth; (d) Pore fracture of the BC after DIOX-H_2 hydrate.

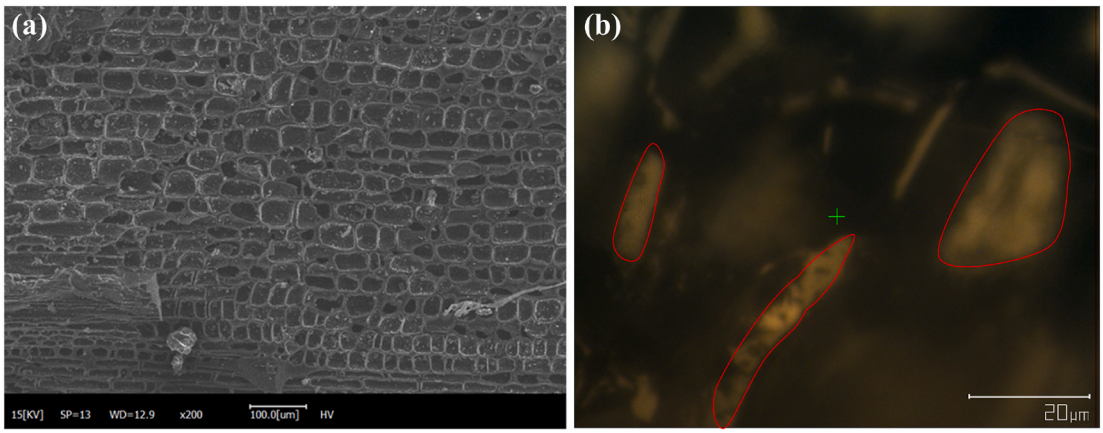

Fig. 11. (a) SEM image of the longitudinal section of dried BC, × 200; (b) Growth morphology of hydrate within the channels of BC at 274.15 K and 18 MPa.

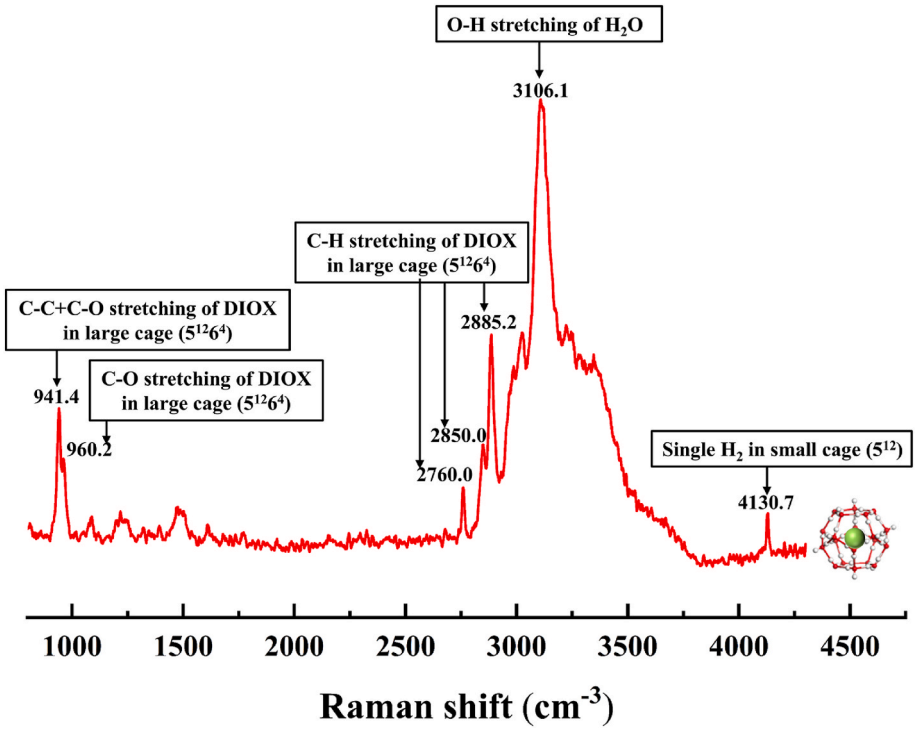

Fig. 12. Raman spectrum of DIOX–H_2 hydrate within the BC's pores at 274.15 K and 18 MPa.

used. The results indicated that, while maintaining a hydrate formation quantity comparable to literature reports, this work exhibited superior hydrogen storage density and rapid hydrogen uptake kinetics. The limited hydrogen storage capacity in prior studies can be attributed to an oversight of the solution's dispersion degree and its correlation with mass transfer resistance. Enhanced dispersion effectively lowers this resistance, directly contributing to the fast kinetics and high density observed in our DIOX-H_2 hydrate system [15,51]. Meanwhile, while reducing the promoter concentration can lower costs, the driving force for hydrogen hydrate formation becomes zero under such conditions [46,52].

Firstly, within the DIOX-H_2 mixed hydrates hydrogen storage systems reported in the literature, the highest hydrogen storage density was achieved with a hydrate formation quantity of merely 5 g. In contrast, this system consistently yielded quantities representing a more than fivefold increase over the highest-density system reported in Table 2, thereby significantly scaling up hydrate production.

Secondly, comparing the hydrogen storage duration, the shortest reported time for the DIOX system was 2 h, achieving a storage density of only 0.286 wt%. Remarkably, this system attained a storage density of 0.670 wt% within the same 2-h period, corresponding to a 134.26% enhancement and a factor of 2.34 times higher than the literature value. To the best of our knowledge, this work reported the highest hydrogen storage capacity for DIOX-H_2 hydrates under comparable conditions.

Furthermore, it is recognized from established hydrate-based hydrogen storage methods that conventional approaches predominantly rely on mechanical agitation to disrupt hydrate films, renew the gas-liquid interface, and generate hydrate particles to increase the interfacial area, thereby aiming to enhance storage density. Conversely, this work directly employed a dispersed solution as the starting point. This novel approach circumvents the energy consumption associated with agitation and eliminates the complexity involved in ice powder preparation, successfully enabling the rapid, high-density formation of DIOX-H_2 hydrates under static conditions.

In summary, this study successfully achieved highly efficient hydrogen storage in DIOX hydrates under static conditions by

Table 2
Hydrogen storage capacity of hydrate formed with IP BC and second-stage hydrogen injection (274.15 K, 18 MPa).

Solution mass(g)	Additives	System	H_2 storage capacity (wt%)[a]	storage rate(wt %/h)[b]	Ref.
10	5.56 mol% ECP hydrate particles	static	0.321	0.161	[15]
32.4	5.56 mol% DIOX	stir	0.286	0.143	[17]
10	C_3H_8 +0.1 wt% SDS	stir	0.628	0.314	[20]
5	5.21 mol% DIOX+0.35mol% THF	stir	0.320	0.160	[29]
10	5.21 mol% DIOX+1.0 wt% L-leucine	stir	0.343	0.172	[52]
3.77	5.56 mol% THF + $-SO^{3-}$@PSNS	stir	0.224	0.112	[21]
20	10 mol%SF_6/90 mol %H_2+ 0.30mol% TBAB	stir	0.484	0.242	[25]
26	5.56 mol% DIOX	stir	0.012	0.006	This work
29.079	5.5 6mol%DIOX,6-12 mm BC	**static**	**0.670**	**0.335**	This work

[a] H_2 storage capacity in 2 h of the hydrate growth phase.
[b] H_2 storage rate in 2 h of the hydrate growth phase.

implementing a strategy combining BC pre-wetting via immersion with a second-stage hydrogen injection method. The attained hydrogen storage density represents a 1.07 to 2.34-fold improvement over literature values, coupled with an exceptionally rapid hydrogen uptake rate of 0.335 wt%/h. This approach provided a simple and efficient solution for hydrate-based hydrogen storage technology, demonstrating promising application potential.

4. Conclusion

This study utilized pre-wetted BC as a porous host to disperse DIOX solution for DIOX-H_2 hydrate formation, enhancing hydrogen storage capacity. FIIR, BET, Raman spectroscopy and SEM revealed the mechanism of BC in enhancing hydrogen storage. The following conclusions are drawn.

(1) BC significantly boosts hydrogen storage density in DIOX-H_2 hydrates, eliminating the induction period and increasing hydrogen storage density from 0.012 wt% to 0.275 wt%.
(2) Second-stage injection elevated hydrogen storage density by 30.9 % via enhanced driving force during mid-late hydrates growth. This achieved a rapid initial uptake rate of 0.952 wt%/h within 0.5 h.
(3) This study presents a BC-enhanced method for hydrate-based hydrogen storage and elucidates the underlying mechanism of this enhancement. Microscopic observation and FTIR revealed that the solution was uniformly distributed within the BC's pores, and the DIOX–H_2 hydrate exhibited a micrometer-scale film-like growth morphology. SEM and microscopy demonstrate that IP strengthens gas-liquid interface area within BC's pores, overcoming heat/mass transfer limitations. Raman spectroscopy analysis revealed single hydrogen molecule occupation in the small cages of DIOX-H_2 hydrate.
(4) Hydrate growth ruptures BC pores, further expanding interfacial area and enabling efficient static storage. However, BC fragmentation impeded cyclic performance. Future work should develop BC-mimetic materials with superior mechanical strength to maintain high hydrogen storage capacity while enabling stable cycling. Furthermore, employing milder promoter via IP could be a viable strategy to achieve high-density and rapid hydrogen storage under more moderate conditions.

CRediT author statement

Zhongming Fan: Formal analysis, Writing–original draft, Data curation; Yanhong Wang: Project administration, Conceptualization, Methodology, Writing–review & editing, Supervision, Funding acquisition; Xuemei Lang: Investigation; Gang Li: Validation; Xinfa Dong: Validation; Shuanshi Fan: Analysis, Theoretical direction, Supervision, Writing - review & editing.

Declaration of competing interest

The authors declare that they have no known competing financial interests or personal relationships that could have appeared to influence the work reported in this paper.

Acknowledgments

This work was supported by the National Natural Science Foundation of China (NSFC), (No. 52576205)

Appendix A. Supplementary data

Supplementary data to this article can be found online at https://doi.org/10.1016/j.ijhydene.2026.154003.

Data availability

Data will be made available on request.

References

[1] Liang Q, Huang Y, Guo Y, Zhang X, Hu X, Zeng H, et al. Efficient osmosis-powered production of green hydrogen. Nat Sustain 2024;7(5):628–39.
[2] Wallington TJ, Woody M, Lewis GM, Keoleian GA, Adler EJ, Martins JRRA, et al. Hydrogen as a sustainable transportation fuel. Renew Sustain Energy Rev 2025;217:115725.
[3] Gupta A, Baron GV, Perreault P, Lenaerts S, Ciocarlan R-G, Cool P, et al. Hydrogen clathrates: next generation hydrogen storage materials. Energy Storage Mater 2021;41:69–107.
[4] Chen B, Qiu F, Xia L, Xu L, Jin J, Gou G. In situ ultrasonic characterization of hydrogen damage evolution in X80 pipeline steel. Materials 2024;17(23):5891.
[5] Hassanpouryouzband A, Joonaki E, Vasheghani Farahani M, Takeya S, Ruppel C, Yang J, et al. Gas hydrates in sustainable chemistry. Chem Soc Rev 2020;49(15):5225–309.
[6] Zhang Y, Bhattacharjee G, Kumar R, Linga P. Solidified hydrogen storage (SolidHyStore) via clathrate hydrates. Chem Eng J 2022;431:133702.
[7] Lang X, Zheng C, Fan S, Wang Y, Li G, Wang S, et al. "Similar self-preservation" and decomposition kinetics of tetrahydrofuran-hydrogen hydrate particles. Int J Hydrogen Energy 2022;47(13):8457–66.
[8] Yan F, Chen H, Chi T, Lu J, Shen X, Xie F, Wang P, Zhang Z. Highly efficient and regenerable amine-impregnated adsorbents: mechanistic insights into glycerol modification for enhanced direct air capture. Chem Eng J 2025;520:166450.
[9] Dai Q, Zhang L, Zhang K, Chen G, Chen Z, Xue X, Wang Y, Wang Z, Di C, Zhao F, Bai J. Carbon-pricing optimization framework for oilfield carbon dioxide-water alternation with economic and environmental gains. Energy Convers Manag 2026;348:120613.
[10] Majid AAA, Worley J, Koh CA. Thermodynamic and kinetic promoters for gas hydrate technological applications. Energy Fuels 2021;35(23):19288–301.
[11] Mao WL, Mao H-k, Goncharov AF, Struzhkin VV, Guo Q, Hu J, et al. Hydrogen clusters in clathrate hydrate. Science 2002;297(5590):2247–9.
[12] Wang P, Chen Y, Teng Y, An S, Li Y, Han M, et al. A comprehensive review of hydrogen purification using a hydrate-based method. Renew Sustain Energy Rev 2024;194:114303.
[13] Florusse LJ, Peters CJ, Schoonman J, Hester KC, Koh CA, Dec SF, et al. Stable low-pressure hydrogen clusters stored in a binary clathrate hydrate. Science 2004;306(5695):469–71.
[14] Lee H, Lee J-w, Kim DY, Park J, Seo Y-T, Zeng H, et al. Tuning clathrate hydrates for hydrogen storage. Nature 2005;434(7034):743–6.
[15] Chen S, Wang Y, Lang X, Fan S, Li G. Rapid and high hydrogen storage in epoxycyclopentane hydrate at moderate pressure. Energy 2023;268:126638.
[16] Lee W, Kang DW, Ahn Y-H, Lee JW. Blended hydrate seed and liquid promoter for the acceleration of hydrogen hydrate formation. Renew Sustain Energy Rev 2023;177:113217.

[17] Zhang Y, Bhattacharjee G, Zheng J, Linga P. Hydrogen storage as clathrate hydrates in the presence of 1,3-dioxolane as a dual-function promoter. Chem Eng J 2022;427:131771.
[18] Xiao M, Zhang J, Li Y, Li Y, Liu X, Wang X, et al. Direct use of simulated seawater achieving superior H_2 gas uptake in H_2-DIOX hydrates for offshore hydrate-based H_2 storage. Int J Hydrogen Energy 2025;169:151041.
[19] Wang P, Li K, Yang J, Zhu J, Zhao Y, Teng Y. Experimental and theoretical study on dissociation thermodynamics and kinetics of hydrogen-propane hydrate. Chem Eng J 2021;426:131279.
[20] Chen S, Wang Y, Fan S, Lang X, Li G. An innovative nucleation method for high and rapid hydrogen storage based on clathrate hydrates. J Mater Chem A 2024;12(19):11424–38.
[21] Kong Y, Wang F, Zhang G, Wang X. Enhanced formation kinetics of mixed H_2/THF hydrate in the presence of nano promoters. Chem Eng J 2023;474:145901.
[22] Bao W, Teng Y, Wang P, Li Y, Zhu J, Han S, et al. Molecular analysis of hydrogen-propane hydrate formation mechanism and its influencing factors for hydrogen storage. Int J Hydrogen Energy 2023;50:697–708.
[23] Maruyama M, Horsfield B, Spangenberg E, Ohmura R, Schicks JM. Interactions between gas hydrate and hydrogen in nature: laboratory evidence of hydrogen incorporation. Int J Hydrogen Energy 2025;184:151927.
[24] Guo Y, Wu W, Hao B, Zheng Q. Formation of hydrogen hydrate in the presence of thermodynamic promoters: a review and prospects. Int J Hydrogen Energy 2024;60:1462–80.
[25] Chen S, Li X, Wang Y, Fan S, Lang X, Lu H, et al. Efficient hydrogen storage in hydrate solid solution: structural insights and performance. Int J Hydrogen Energy 2026;204:153331.
[26] Kawamura T, Takeya S, Ohtake M, Yamamoto Y. Enclathration of hydrogen by organic-compound clathrate hydrates. Chem Eng Sci 2011;66(11):2417–20.
[27] Zhang Y, Bhattacharjee G, Dharshini Vijayakumar M, Linga P. Rapid and energy-dense methane hydrate formation at near ambient temperature using 1,3-dioxolane as a dual-function promoter. Appl Energy 2022;311:118678.
[28] Bhattacharjee G, Goh MN, Arumuganainar SEK, Zhang Y, Linga P. Ultra-rapid uptake and the highly stable storage of methane as combustible ice. Energy Environ Sci 2020;13(12):4946–61.
[29] Kong Y, Yu H, Liu M, Zhang G, Wang F. Ultra-rapid formation of mixed H2/DIOX/THF hydrate under low driving force: important insight for hydrate-based hydrogen storage. Appl Energy 2024;362:123029.
[30] Nguyen NN, Nguyen AV. "Nanoreactors" for boosting gas hydrate formation toward energy storage applications. ACS Nano 2022;16(8):11504–15.
[31] Lee W, Kim M-K, Moon S, Lee JW, Ahn Y-H. Rapid hydrogen enclathration and unprecedented tuning phenomenon within superabsorbent polymers. Appl Energy 2025;377:124367.
[32] Kang DW, Lee W, Ahn Y-H, Lee JW. Confined tetrahydrofuran in a superabsorbent polymer for sustainable methane storage in clathrate hydrates. Chem Eng J 2021;411:128512.
[33] Deng Z, Fan S, Wang Y, Lang X, Li G. Enhance hydrates formation with stainless steel fiber for high capacity methane storage. Chin J Chem Eng 2022;50:435–43.
[34] Zhang Y, Fan S, Wang Y, Lang X, Li G. Enhanced methane hydrate formation through lignocellulose fiber. Fuel 2025;380:133194.
[35] Carrillo-Carrión C, Farrando-Perez J, Daemen LL, Cheng YQ, Ramirez-Cuesta AJ, Silvestre-Albero J. Zr-porphyrin metal–organic framework as nanoreactor for boosting the formation of hydrogen clathrates. Angew Chem Int Ed 2024;63(6):e202315280.
[36] Laalam A, Bazazi P. Holding the invisible: advanced materials for hydrogen storage. I Int J Hydrogen Energy 2025;169:151057.
[37] Farrando-Perez J, Balderas-Xicohtencatl R, Cheng Y, Daemen L, Cuadrado-Collados C, Martinez-Escandell M, et al. Rapid and efficient hydrogen clathrate hydrate formation in confined nanospace. Nat Commun 2022;13(1):5953.
[38] Kummamuru NB, Ciocarlan R-G, Houlleberghs M, Martens J, Breynaert E, Verbruggen SW, et al. Surface modification of mesostructured cellular foam to enhance hydrogen storage in binary THF/H2 clathrate hydrate. Sustain Energy Fuels 2024;8(13):2824–38.
[39] Yang L, Fan S, Wang Y, Lang X, Xie D. Accelerated formation of methane hydrate in aluminum foam. Ind Eng Chem Res 2011;50(20):11563–9.
[40] Khan MN. Hydrogen as future sustainable energy resource: an insight into technological advancements in hydrate-based hydrogen storage. Int J Hydrogen Energy 2024;97:151927.
[41] Watson G, Kummamuru NB, Verbruggen SW, Perreault P, Houlleberghs M, Martens J, et al. Engineering of hollow periodic mesoporous organosilica nanorods for augmented hydrogen clathrate formation. J Mater Chem A 2023;11(47):26265–76.
[42] Casco ME, Rey F, Jordá JL, Rudić S, Fauth F, Martínez-Escandell M, et al. Paving the way for methane hydrate formation on metal–organic frameworks (MOFs). Chem Sci 2016;7(6):3658–66.
[43] Wang J, Li Z, Li Y, Wang Z, Liu Xe, Liu Z, et al. Evolution and correlation of the physiochemical properties of bamboo char under successive pyrolysis process. Biochar 2024;6(1):33.
[44] Aljeban N, Alanazi A, Abdelgawad K, Barri AA, Al Hamad J, Hoteit H. Solubility and interfacial tension of hydrogen and hydrogen-methane mixtures in water: effect of pH, salinity, and gas composition. Int J Hydrogen Energy 2026;204:153276.
[45] Hasegawa T, Brumby PE, Yasuoka K, Sum AK. Mechanism for H_2 diffusion in sII hydrates by molecular dynamics simulations. J Chem Phys 2020;153(5).
[46] Zhang J, Li Y, Li Y, Xiao M, Rao Y, Linga P, et al. Phase equilibria and guest gas occupancy characteristics of H_2-DIOX sII hydrates based on calorimetric and Raman analysis. Fluid Phase Equilib 2025;589:114262.
[47] Jena L, Soren D, Deheri PK, Pattojoshi P. Preparation, characterization and optical properties evaluations of bamboo charcoal. Curr Re Green Sustain Chem 2021;4:100077.
[48] Roodbari SK, Mohebbi V, Behbahani RM. Prediction of gas hydrates phase equilibrium in porous media – pore size effect and thermodynamics approach. Fluid Phase Equilib 2025;593:114330.
[49] Hashimoto S, Sugahara T, Sato H, Ohgaki K. Thermodynamic stability of H_2 + tetrahydrofuran mixed gas hydrate in nonstoichiometric aqueous solutions. J Chem Eng Data 2007;52(2):517–20.
[50] Zhang J, Li Y, Rao Y, Li Y, He T, Linga P, et al. Probing the pathway of H2-THF and H2-DIOX sII hydrates formation: implication on hydrate-based H_2 storage. Appl Energy 2024;376:124289.
[51] Kim K, Lee W, Lee J, Lee JW. Water-in-oil emulsions as micro-reactors for achieving extremely rapid and high hydrogen uptakes into clathrate hydrates. Chem Eng J 2024;499:156666.
[52] Xiao M, Hondo E, Zhang Y, Yin Z, Linga P. Leucine-enhanced sII hydrate kinetics for hydrogen storage. Energy Fuels 2025;39(13):6620–32.